metals

Article

Ultrasonic Resonance Fatigue Testing of 6082 Aluminum Alloy

Diyan M. Dimitrov [1,*], Stoyan D. Slavov [2], Desislava Y. Mincheva [3] and Adélio M. S. Cavadas [4]

[1] Department of Mechanics and Machine Elements, Technical University of Varna, Studentska 1 str., 9010 Varna, Bulgaria
[2] Department of Manufacturing Technologies and Machine Tools, Technical University of Varna, Studentska 1 str., 9010 Varna, Bulgaria; sdslavov@tu-varna.bg
[3] Department of Materials Science and Technology, Technical University of Varna, Studentska 1 str., 9010 Varna, Bulgaria; dmincheva@tu-varna.bg
[4] Escola Superior de Tecnologia e Gestão, Instituto Politécnico de Viana do Castelo, Avenida do Atlântico 644 str., 4900-348 Viana Do Castelo, Portugal; adelioc@estg.ipvc.pt
* Correspondence: dm_dimitrov@tu-varna.bg; Tel.: +359-878148125

Abstract: This study explores the fatigue properties of EN AW-6082-T6 aluminum alloy in the gigacycle range (10^6–10^9 cycles), using ultrasonic resonance fatigue testing at 20 kHz in a push–pull mode with a symmetric load cycle (R = −1). A custom-built ultrasonic fatigue machine, developed at TU-Varna, comprising a generator, ultrasonic train (including a high-power transducer, booster, custom-made sonotrode, and specimen), monitoring, data logging systems, and an air-cooling capability, was used for the experiments conducted. A Bezier curve sonotrode, with an amplification ratio of 1:6, was designed and produced for the test. Hourglass-shaped specimens were designed on the base of the dynamic Young's modulus E = 71.3 GPa, determined through the impulse resonance method (ASTM E1876-01), and validated with FEM analysis for resonance length and stress amplitude. The fatigue testing revealed a fatigue strength reduction of approximately 60 MPa between 10^6 and 10^9 cycles. The percentile of failure curves based on a Cactillo–Canteli model fits well with the experimental data and gives a fatigue limit at 10^9 cycles σl = 104 MPa and "endurance strength" σw = 84 MPa. Surface crack initiation was consistently observed with predominately cleavage transgranular fractures in the fatigue zone. The present research highlights the utility of ultrasonic testing for examining fatigue behavior in the gigacycle regime.

Keywords: ultrasonic fatigue; VHCF; sonotrode; aluminum alloy; fatigue fracture; S-N curve

check for updates

Academic Editor: Dariusz Rozumek

Received: 13 December 2024
Revised: 9 January 2025
Accepted: 12 January 2025
Published: 27 January 2025

Citation: Dimitrov, D.M.; Slavov, S.D.; Mincheva, D.Y.; Cavadas, A.M.S. Ultrasonic Resonance Fatigue Testing of 6082 Aluminum Alloy. *Metals* **2025**, *15*, 127. https://doi.org/10.3390/met15020127

1. Introduction

Nowadays, with the development of ultrasonic resonance fatigue testing techniques, it is possible to answer the question "Is there an infinite fatigue life?" [1]. The reasonable limit of conventional fatigue machines is about 10^6–10^7 cycles. The range beyond 10^7 cycles is called gigacycle fatigue or very high cycle fatigue (VHCF). It can be explored by ultrasonic equipment, working at 20 kHz. With such equipment, a fatigue life of 10^{10} cycles can be reached within a reasonable time (~6 days).

The problems and challenges in ultrasonic resonance testing arise from the test setup. The specimens have to be designed with a half standing wave (λ/2) length such that the middle section is a displacement node. This length depends on the material density and elastic properties, so there is no standard shape or dimensions for the test specimens. Each test needs a custom-designed specimen. When determining the type and size of the stress concentrator, the mechanical properties of the tested material and the capabilities of the ultrasonic train components (mainly the amplification horn, i.e., the sonotrode, which is usually custom-designed) must be considered in order to develop the displacement amplitudes needed for the test. The heating during the test depends on the acoustic impedance of the materials, so a proper cooling system must be created for the test. Using additional elements, the ultrasonic fatigue tester machine can be modified so as to provide tests with an unsymmetrical loading cycle, torsional or three-point bending fatigue, as well as high- and low-temperature tests [2–4].

Researchers in VHCF have found out that there are fatigue fractures beyond 10^7 cycles even for materials with BCC lattice, like high-strength alloyed steels. For a lot of steels, the fatigue fracture initiation site is under the surface, around a defect, an inclusion or a pore.

For annealed ductile metals, like Cu and Al, there is a conventional fatigue limit at 10^7 cycles, but beyond 10^8 cycles, an increase in surface roughness, due to reversible stress, is detected. This can form local stress concentrations capable of developing persistent slip bands as well as a fatigue crack [2,3].

For alloys of FCC metals, like Al alloys, Cu alloys and stainless steels, as well as Mg alloys with the presence of defects, intermetallic inclusions and pores, classified as type II, even at higher temperature or in corrosive environments, it is supposed that there is no infinite fatigue limit [4,5].

In [6], a comprehensive review of ultrasonic fatigue testing of additively manufactured materials, such as Ti, cast Al alloys and stainless steels, is presented. The origin of a fatigue fracture, in most cases, is a process-induced defect. This shows the increasing application of the method.

Usually, the results from the S-N diagram are fitted to the Basquin equation and a second line with a lower slope is formed in the VHCF region. The slope change is within around 10^6 cycles [7–9]. In recent years, the percentile curves models, based on the Weibull distribution, have become popular.

Alloys of the Al-Mg-Si system can be dispersion-hardened by quenching and subsequent aging. The wrought alloy AW 6082 is a medium- to high-strength alloy from this group with excellent corrosion resistance. It is known as a structural alloy, used for various structural elements of critical importance in aviation, automotive, transport, military, shipbuilding, civil engineering, and other industries. The heat treatment of this alloy can form various mechanical properties due to type, shape and size of the precipitates. In [10,11], various types of intermetallic particles are identified by SEM and TEM microscopy. The variation of tensile strength, yield strength, elongation and fracture toughness at varying temperatures and time for artificial aging is discussed. It is concluded that strength is primarily affected by the intermetallic precipitate (GP zones -β″-β′). The fracture toughness essentially depends on the temperature and the aging time. The Mg/Si ratio of the particular batch is also found to be important in order to type the shape and size of the precipitated intermetallic particles [12]. Other authors establish the effect of the strain rate of hot deformation on hardness and peak aging time [13].

Various types of fracture modes in the VHFC region, including interior crack initiations, of these type of materials, like slip bands, interior inclusion (fish-eye), are summarized in the review paper in [14]. In [15], the featureless subsurface crack initiation in AW 6082 aluminum alloy is observed. The size effect is studied in [16] and a model parameter capable of incorporating this effect is suggested. Fatigue fractures beyond 10^9 cycles are registered.

Taking into account the review above, it is reasonable to suppose that the fatigue life of this alloy is also a complex phenomenon, and the simple empirical correlations of the fatigue strength with the tensile or the yield strength are dubious. On the other hand, in industrial conditions, many technological factors of the production cycle of wrought Al alloys can lead to microstructure and property variations [12]. The aim of this article is to contribute to the topic by preparing a proper ultrasonic 20 kHz resonance test setup and presenting fatigue results in the gigacycle area of EN AW6082-T6, as well as to study fatigue fracture surfaces.

2. Materials and Methods

2.1. Material Properties

The specimens are prepared from an extruded rod with a diameter ϕ12 mm, with heat treatment T6, quenching and artificial aging. The chemical composition, measured on the cross-section by SEM -EDX by Hitachi VP-SEM SU1510 (Hitachi High Technologies America, Inc., Tokyo, Japan) and in accordance with EN 573-3, is given in Table 1. It is seen that for the particular batch, the Mg content is very high and the Si content is at the lowest possible level.

Table 1. Chemical composition of the AW 6882-T6 (wt. %).

6082	Mg	Mn	Fe	Si	Cu	Zn	Cr	Ti	Al
Current	1.41	0.51	0.01	0.68	0.006	0.19	0.18	-	Balance
EN 573	0.6–1.2	0.4–1.0	≤0.5	0.7–1.3	≤0.1	≤0.2	≤0.25	≤0.25	Balance

In the microstructure analysis, Keller's solution (Gündüz Kimya, İstanbul, Turkey) was used for etching. The composition of Keller's solution is 0.5% hydrofluoric acid (HF) in 50 mL of water. The microstructural features were observed by using an XJL-200 optical microscope (Opassy Industry Group Co., Ltd., Dongguan, China). The main alloying elements in aluminum alloys are magnesium and silicon, with Mg_2Si serving as one of the dispersion strengthening phases. The primary phase consists of α-solid solution crystals of aluminum, which appear as white regions under the microscope. Course and fine intermetallic phase precipitates, including Mg_2Si, are observed at the grain boundaries and appear as dark regions in the micrograph, as shown in Figure 1a,b. The SEM photographs give a better view of the size, type and the distribution of the intermetallic phases, as shown in Figure 1c,d. Such observations in the structure of the base metal have also been reported by other authors [11,17].

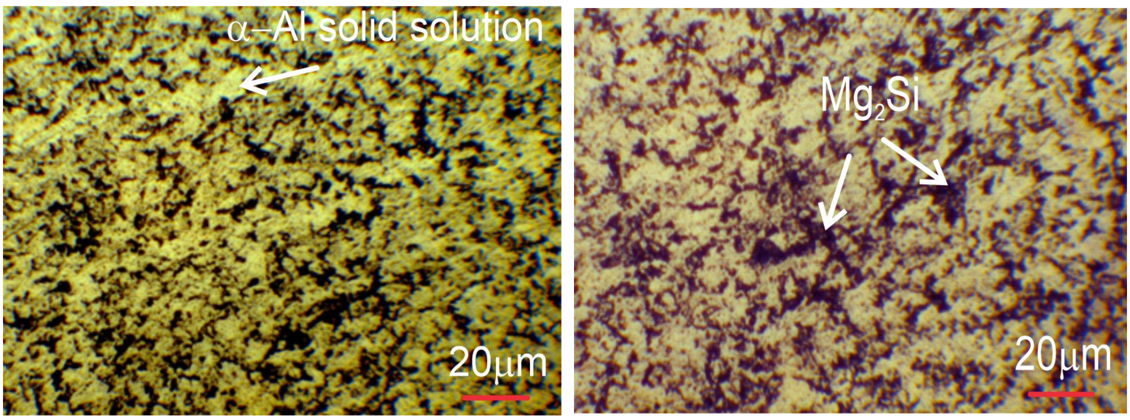

(a) (b)

Figure 1. *Cont.*

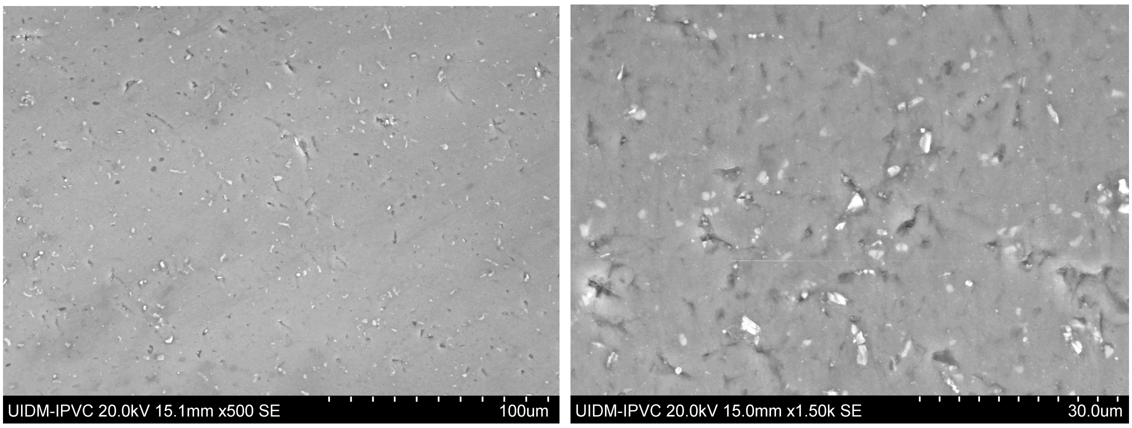

(c) **(d)**

Figure 1. Microstructure of the AW 6082-T (light optical microscope: (**a**,**b**) fragments; SEM (**c**,**d**)).

The Vickers method, with a load of 50 g, was used to measure the microhardness of the structure. The microhardness measured in the α-Al is in the range of 90 ± 1 HV0.05, as shown in Table 2. Tensile tests are carried out, using Shimadzu—AG-X Plus 100 kN (a universal testing machine, Shimadzu Corporation, headquartered in Kyoto, Japan) at room temperature. Dog bone specimens, with a gauge diameter d_0 = 10 mm and gauge length L_0 = 50 mm in accordance with the proportions recommended in the ISO 6892 standard [18], are machined from the rods. A total of three specimens are tested, and the results calculated are presented in Table 2. The uncertainties given are expanded by a factor of 2 to cover the 95% range.

Table 2. Tensile properties and hardness AW 6882-T6.

Tested Material	Rp, 0.2, MPa	Rm, MPa	A, %	HV0.05
6082-T6	268 ± 5	298 ± 4	6.8 ± 0.6	90 ± 1

2.2. Ultrasonic Resonance Fatigue Testing Device

The fatigue testing device is designed and assembled by the team from Strength of Materials laboratory of Technical University of Varna. It consists of an ultrasonic resonance unit and monitoring and control unit, as shown in Figure 2.

The ultrasonic train is adjusted to work in resonance conditions, at 20 ± 0.5 kHz. The generator (1) drives the high-power piezo converter (2). The booster design is with a wide flange in the middle nodal point to fix the ultrasonic train to the foundation. The difference between the inlet and outlet diameter gives the amplification of the vibration an amplitude of 1:1.5. The sonotrode (4) is a custom-designed piece, made of Ti6Al4V, which concentrates the vibration energy at the end. The design with the Bezier curved profile is chosen to meet the test requirements (see Section 2.3). The specimens (6) for the resonance fatigue test are also custom-designed. The shape of the stress concentrator and the total length depend on the elastic (E, ν), physical (ρ) and mechanical properties of the material. Usually, the density of the piece material for testing is close to the theoretical one, but the Young's modulus can vary by about 5% compared to the reference value, which results in about a 3 mm difference in the overall specimen length. A similar conclusion is given in [19]. It is recommended that the Young's modulus be determined by a non-destructive dynamic method, such as obtaining the frequency of the fundamental bending of the axial mode of a free-free beam by impulse excitation of vibration (IET), directly on the blank rods, ASTM E1876. The monitoring and control systems are, respectively, a resonance control loop provided by the generator itself. The cycle counting system consists of a dynamic strain gauge (PVDF material) (5) glued to the sonotrode and a comparator unit, which transforms the harmonic signal to easy for counting pulses. The vibration amplitude at the end of the specimen is monitored by a fiberoptic sensor (9). Since the fiberoptic sensor is sensitive to the surface quality, in order to ensure the reproducibility of the measurements from specimen to specimen, at the free end of the specimen tested, a thin mirror surface foil is glued.

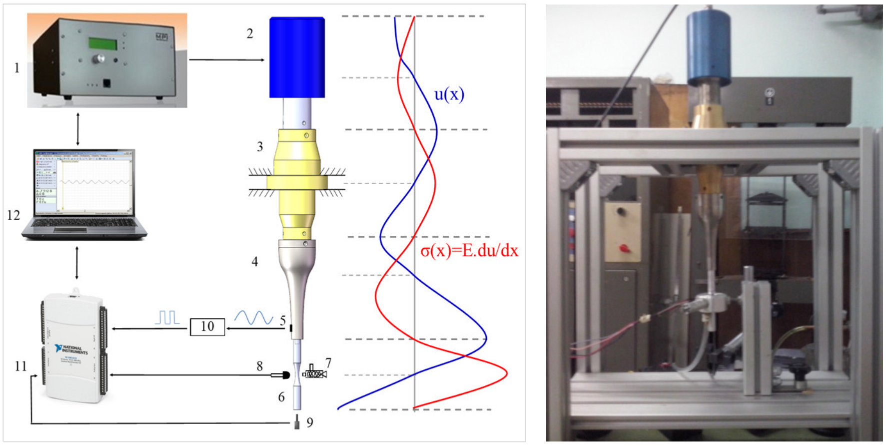

(a) **(b)**

Figure 2. Ultrasonic resonance 20 kHz fatigue test unit, designed in Strength of Materials Lab in TU-Varna: (**a**) block scheme; (**b**) physical device; u(x)—axial displacement amplitude; σ(x) = E.du/dx normal stress amplitude. (1)—Generator 1 kW (MPI Ultrasonics, Switzerland); (2)—high-power piezo-ceramic transducer (MPI Ultrasonics, Switzerland); (3)—Booster Gold (1:1.5); (4)—Bezier sonotrode Ti4Al6V; (5)—dynamic strain gauge (PVDF foil); (6)—specimen; (7)—vortex tube; (8)—IR thermometer (MLX90614); (9)—fiberoptic sensor (Philtec D20); (10)—comparator; (11)—ADC (NI 6216); (12) computer with LabView.

During the test, the temperature in the specimen can increase due to the damping, which is why a cooling system is added. It consists of a vortex tube (7) and an IR pyrometer (8). The vortex tube is a good solution for spot cooling. It has no moving parts. When supplied with compressed air, the vortex reservoir divides the air into a hot and a cool flow. The IR sensor gives accurate results if the surface of the specimen is black, so before testing, each specimen is sprayed with black paint in the middle.

The signals from all the sensors are fed to an ADC (NI 6216-16bit multifunctional ADC with a sampling rate of up to 200 kS/s). A LabView routine controlling the fatigue test is created. It monitors the displacement at the free end, the temperature and counts the load cycles. Based on values measured, it controls the generator power and the working time. The fatigue testing is carried out in pulse–pause (1–0.5) regime. If the temperature increases the upper limit, the cooling system is switched on. The test is stopped when the generator is not able to maintain the resonance conditions.

2.3. Design and Machining the Sonotrode Part

Because the sonotrode part (position 4 in Figure 2) must concentrate the vibration energy and amplify the amplitude of the vibrations at its front end to certain values, it must be of a suitable shape and dimensions. Considering the material properties (E = 124 GPa, $\rho = 4450\ \mathrm{kg/m^3}$, measured on a blank), the dimensions of the fatigue test specimens, and the resonant frequency of 20.0 ± 0.5 kHz that must be maintained during the fatigue test, the contour shape and dimensions were determined using the Cubic Bézier curve, which has the following explicit form [20]:

$$B(t) = (1-t)^3 \cdot P_0 + 3 \cdot (1-t)^2 \cdot t \cdot P_1 + 3 \cdot (1-t) \cdot t^2 \cdot P_2 + t^3 \cdot P_3, \quad (1)$$

where $0 \leq t \leq 1$ are the t-coordinates of the control points, and P_i ($i \in 0 \ldots 3$) are the values of these control points.

To obtain the complex contour shape needed for the sonotrode in real life, a suitable piece of CNC lathe equipment should be used [21]. To obtain a suitable numerical control (NC) code for it using Equation (1), it is necessary to convert it into parametric functions that correspond to the CNC-machine coordinate axes. In the present case, these axes are designated as X (movement in radial direction) and Z (movement in axial direction and coincident with the lathe machine spindle axis). Thus, the function from Equation (1) was transformed into a pair of functions, which are used to calculate the coordinates of the toolpath of the CNC-machine that is needed to end the machining of the sonotrode contour. They are as follows:

$$\begin{cases} X_n = (1-t_n)^3 \cdot X_0 + 3 \cdot (1-t_n)^2 \cdot t_n \cdot X_1 + 3 \cdot (1-t_n)^1 \cdot (t_n)^2 \cdot X_2 + (t_n)^3 \cdot X_3 \\ Z_n = (1-t_n)^3 \cdot Z_0 + 3 \cdot (1-t_n)^2 \cdot t_n \cdot Z_1 + 3 \cdot (1-t_n)^1 \cdot (t_n)^2 \cdot Z_2 + (t_n)^3 \cdot Z_3 \end{cases} \quad (2)$$

where n ($n \in 0..n_{max}$) is the index of the variable $t_n = \frac{n}{n_{max}}$ that represents the t-coordinates ($0 \leq t_n \leq 1$) for which the profile curve coordinates are calculated; n_{max} is an integer, which sets the number of the intermediate points of the toolpath; X_i and Z_i ($i \in 0...3$) are the coordinates of the Bézier's control points along the CNC-machine's X and Z axes.

The values of the parameters X_i and Z_i in Equation (2) are obtained after the finite element analysis (FEA) conducted to achieve a suitable contour shape of the sonotrode that will ensure maximum resonance conditions at the 20.0 ± 0.5 kHz interval (see Figure 3a), and stress distribution from the axial harmonic load (see Figure 3b) by applying numerical optimization procedures, like the ones suggested in [22].

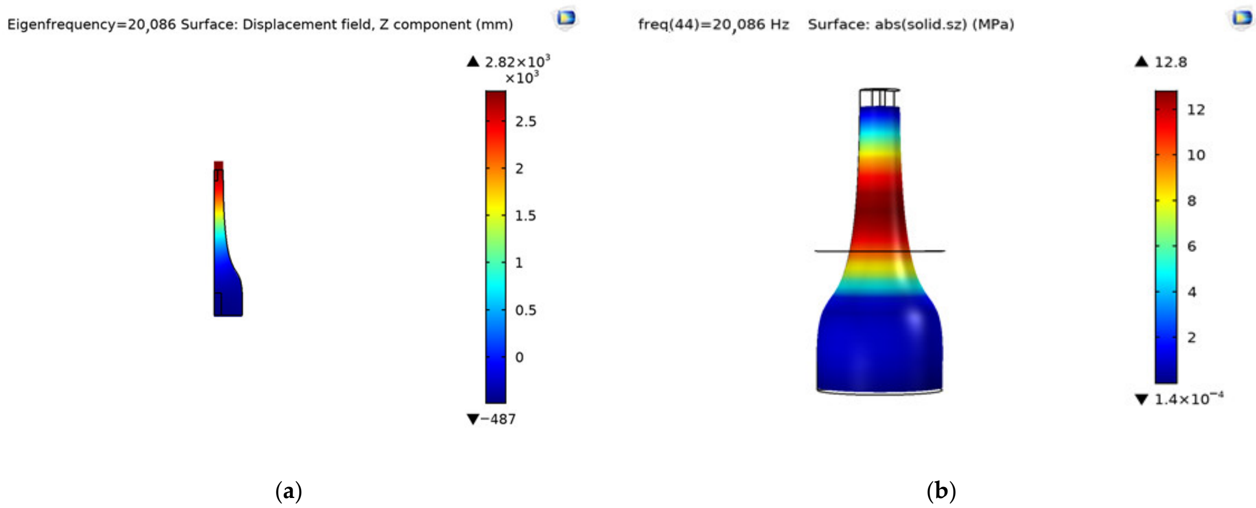

Figure 3. Sonotrode design. (**a**) Axial modal shape close to 20 kHz; (**b**) stress distribution from axial harmonic load caused by unit displacement at the higher diameter phase.

A possible solution is found when the X_i and Z_i parameters have values (in millimeters) as follow: $X_{0\cdots3} = 25; 26; 8; 8$, and $Z_{0\cdots3} = 10; 60; 10; 129.5$. This solution gives the eigenfrequency 20,086 kHz, which is a negligible difference from the required 20 kHz, an amplification factor of about 1:6 and maximum stress 12.8 MPa per unit displacement amplitude on the input face. The important detail in FEA simulation is that the mounting studs on each end of the sonotrode can affect the eigenfrequency, so they are included as follows: a steel stud with 0.5″ diameter, and 20 mm length for mounting to the booster and an aluminum alloy 6082 stud M6 × 10 mm to mount the specimen.

The manufacturing of a real sonotrode with a contour shape, as close as possible to that calculated by Equation (2), can be carried out by using a two-axis CNC (computer numerical control)-lathe machine (FANUC 0i-Mate TC). For this purpose, an equation-driven spline curve (see positions 1 and 2 in Figure 4) is created, firstly in a CAD modeler SOLIDWORKS 2024 (SolidWorks Corporation, Waltham, MA, USA), using the numerical parameters $X_{0\ldots3}$ and $Z_{0\ldots3}$ from Equation (2). It is used to create a revolved 3D sonotrode solid model, as shown in pos. 3. At the next stage (pos. 4), the obtained 3D model is processed by CAMWorks 2024 (HCL GmbH, Eschborn, Germany), turning the module to set-up and adjusting the corresponding operation parameters for the lathe machining. The NC code for driving the CNC lathe is generated automatically by the CAM software, using the corresponding postprocessor, which is adjusted precisely, according to the FANUC 0i-Mate TC capabilities for performing canned cycles for rough (G71) and finish (G70) turning operations (see pos. 5). Then, the physical sonotrode is processed, following the instructions from the NC obtained in this way (see pos. 5).

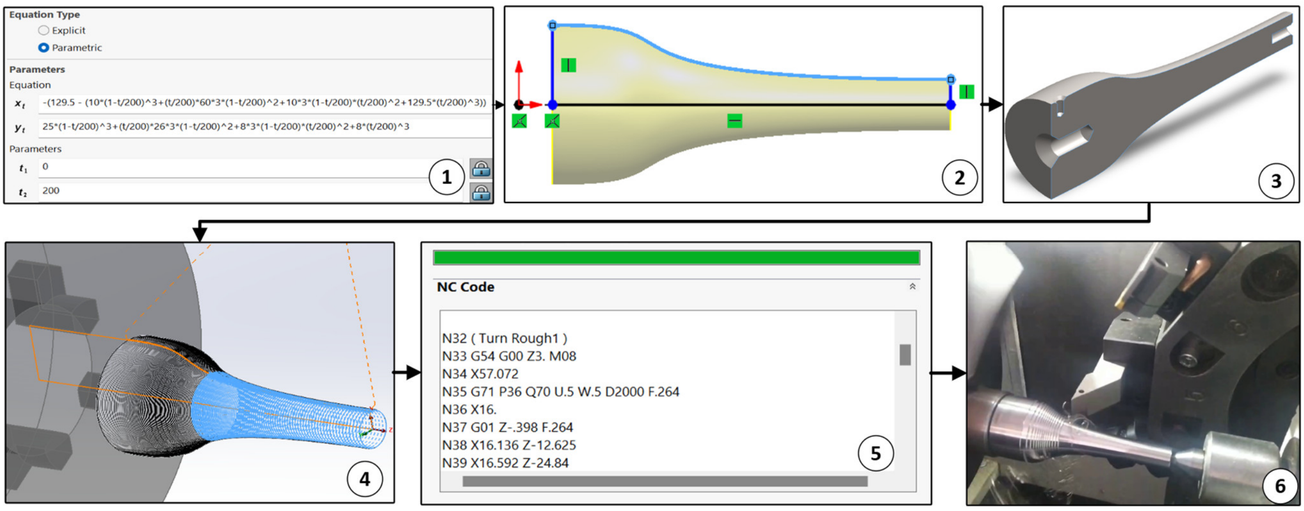

Figure 4. Steps for obtaining sonotrode with optimal shape and dimensions, using CAD/CAM software.

As can be seen in Figure 4 pos. 5, the toolpath is divided into linear segments, starting from block N37 and proceeding to the end of the sonotrode contour toolpath. Decreasing the deviations of the contour shape means increasing the linear segment number and shortening their lengths, which is controlled by parameter n_{max}; see Equation (2). In the present case, the number of the linear segments is chosen to be $n_{max} = 200$ to achieve optimal balance between the sonotrode profile accuracy and the length of the NC program.

To examine the resonance behavior, the sonotrode manufactured was tested with real specimens on the fatigue testing setup. The results confirm that its shape and dimensions are suitable to achieve and maintain the desired resonance frequency within the allowable tolerance for a long period of time.

3. Results and Discussion

3.1. Specimen Design

Pieces of ∅10 × 200 mm are machined from the initial rod. The impulse excitation technique provides the result for the dynamic Young's modulus, independent of the Poisson coefficient E_d = 71.3 GPa, Table 3. As an example of variation of the E values, in [23], E = 77 GPa is reported. The density measured by the water displacement method is ρ = 2707 kg/m^3, as shown in Table 3.

Table 3. Elastic properties and density of rods, extruded from AW 6082-T6.

Tested Material	Ed *, GPa	Poisson Ratio, ν **	Density, ρ ***, kg/m^3
6082-T6	71.3 ± 0.6	0.33	2707 ± 9

* Calculated from the bending mode frequency according to ASTM. ** Accepted value for Al alloys. *** Calculated by the water displacement method.

For a specimen with a hemispherical concentrator, there is a similar form solution for calculating the resonance length, resembling a concentrator with a hyperbolic cosine function [24,25]. A specimen with a total length of 91.4 mm is designed according to this similar form solution, as shown in Figure 5a.

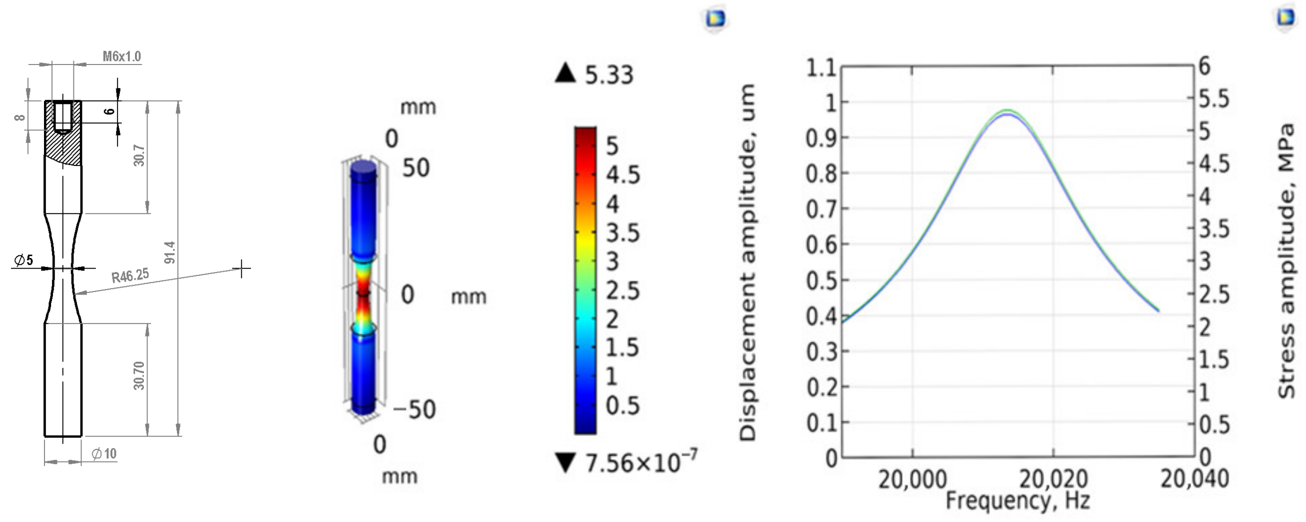

(**a**) (**b**) (**c**)

Figure 5. Specimen design and stress FEM modal solution: (**a**) specimen drawing; (**b**) normal stress distribution under boundary load in axial direction at the free end, resulting in 1µm displacement amplitude at frequency of f = 20,014 Hz; (**c**) variation of axial displacement amplitude and the free end and maximal stress amplitude at the middle section in the vicinity of the resonance.

The dimensions proposed are approved by FEM solution, created with Comsol Myltuphysics, using the material properties in Table 3. The eigenvalue solution gives the exact eigenfrequency of f = 20,014 kHz, which is a negligible difference from the initial value of 20 kHz. The range around this frequency is explored using modal analysis. For this analysis, a linear elastic material model with damping η = 0.001, expressed as "isotropic loss factor", is created. A boundary load in the axial direction is applied at the end of the specimen, so that the resulting displacement amplitude at resonance to be approximately 1µm, as shown in Figure 5c. The resulting maximal stress amplitude is 5.33 MPa/µm, as shown in Figure 5b. This value is used as a stress constant to convert the displacement of the free end of the specimens measured in MPa. As can be seen, the displacement amplitude and the stress amplitude are proportional, as shown in Figure 5c. At one of the ends of the machined specimen, the threaded hole is drilled in order to be able to mount it to the sonotrode using a stud. The final stress calibration is performed with a miniature strain gauge glued to the nodal point of the specimen.

3.2. Fatigue Results

Fatigue tests are carried out in an axial tension–compression mode with a symmetrical load cycle R = −1. The purpose is to establish the influence of the stress amplitude (σ_a) on cycles-to-failure (N), i.e., the fatigue life in the gigacycle range from 10^6 to 10^9 cycles. The specimens, which did not break until 10^9 cycles, are considered survivals. The results are plotted in the S-N diagram shown in Figure 6. It is clear that the specimens continue to fracture beyond 10^7 cycles, and even beyond 10^8 cycles. The difference between the fatigue limit at 10^6 cycles and 10^9 cycles seems to be about 60 MPa.

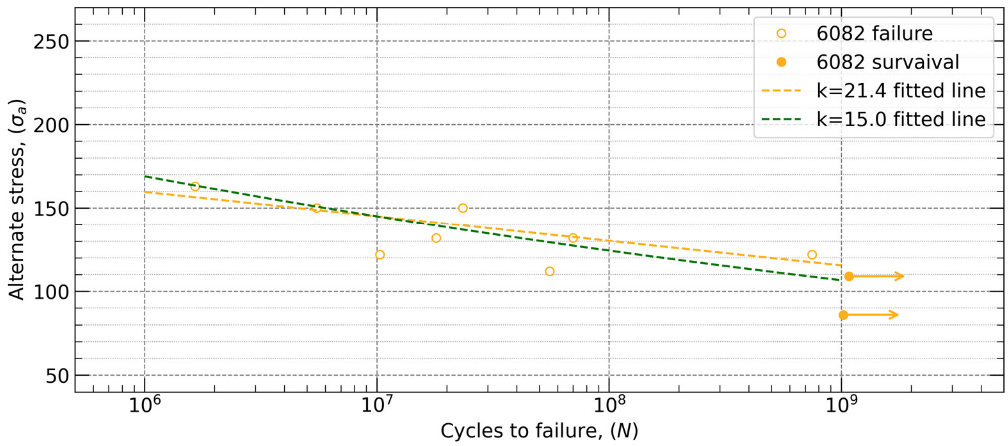

Figure 6. Results from the fatigue test at 20 kHz (semilog plot) and fitted S-N curve in gigacycle range for EW 6082 -T6 with slopes k = 21.4 and k = 15.

Two of the specimens, tested at stress amplitudes 109 MPa and 86 MPa, survived 10^9 cycles. One specimen fatigued at 122 MPa, reaching 10^7 cycles. It seems to be an outlier, and its fractured surface will be carefully analyzed below. The regression lines in log-log scale are determined according to Basquin's Equation (3), which can also be presented as a function of the number of cycles N (3) and as a line equation in log-log scale (4).

$$\sigma_a = \sigma_f \cdot (N)^{-b}, \qquad N = \left(\frac{\sigma_f}{\sigma_a}\right)^k \tag{3}$$

$$logN = A - k.log\sigma_a \tag{4}$$

where σ_f—fatigue strength parameter; $k = \frac{1}{b}$, $A = k.log\sigma_f$—slope and intercept parameter of the line in log-log scale

Unknown slope and intercept parameters are fitted by maximizing the likelihood function (5), which incorporates the right censored results from the survivals with adding the probability of the survival part for them [26].

$$L(\theta|Data) = \prod [f_w(w_i|\theta)]^{\delta_i} [1 - F_W(w_i|\theta)]^{1-\delta_i}, \tag{5}$$

$f_w(w|\theta)$, $F_W(w|\theta)$ are the PDF, CDF of a Normal (Gaussian) distribution; $\theta = \left(\mu_i,\ s^2\right)^T$ is a vector with Normal distribution parameters, where the mean is $\mu_i = logN_i = A - k.log\sigma_a$; s is the standard deviation of the fatigue life; $\delta_i = \left\{ \begin{matrix} 1 - fracture \\ 0 - survival \end{matrix} \right\}$.

Considering the Gaussian distribution of dependent variable $w_i = logN_i$ at a certain stress amplitude $\sigma_{a,i}$, three unknowns must be found. To infer the unknowns A, k, s, a Bayesian approach is employed. Initially, prior distributions for these unknowns are selected, and posterior data ($posterior \sim likelihood \times prior$) are numerically obtained via

Markov Chain Monte Carlo (MCMC) sampling, utilizing appropriate algorithms such as Hamiltonian Monte Carlo or Metropolis–Hastings, among others [27].

For experimental data, vague Normal distribution priors are assigned to A and k and Half-Normal for standard deviation parameter s, given that positive values ($s > 0$) are required.

After sampling, a broad and multimodal posterior distribution for the slope parameter (k) is observed, with a peak around 7 and sharper peaks around 15 and 20. To refine the model, reference results are incorporated in the prior distribution. The FKM guidelines [28] propose for wrought Al alloys a general double slope with slope parameters k_I = 5 and k_{II} = 15 and knee point at $N = 10^6$ cycles. The experimental results from the fatigue testing of AW 6082, marked as a base material at 20 kHz, shown in [8], fit the VHCF region with a slope parameter k = 22. These slope values align with our observed peaks, so the probabilistic model is refined by choosing a tight (strong) prior for k initially with mean 15 and subsequently with mean 22 and a standard deviation equal to 1. The resulting best fit parameters, together with their 95% high-density intervals (HDIs) and values of log-likelihood function, are given in Table 4. Posteriors of k align with the strong prior, centering around the prior mean and having 95% HDI that spans ±2 *standard deviation*.

"The posterior distribution of (k) a 95% highest density interval (HDI) ±2 standard deviations". Comparing the negative values of log-likelihood function, evaluated with the best fit parameters, the slope k = 21.4 gives a slightly lower value, indicating slightly better fit of the experimental data.

Table 4. The resulting best fit parameters, together with their 95% high-density intervals (HDIs) and values of log-likelihood function.

Prior	Parameter	Posterior			Likelihood Value
		Mean Value	**95% HDI**		**−log (*L*)**
N (40, 10^2)	A	39.42	34.55	44.09	9.153
N (15, 1^2)	k	15.00	12.84	17.27	
HN (5^2)	s	0.844	0.434	1.422	
N (40, 10^2)	A	53.04	47.83	57.09	8.427
N (22, 1^2)	k	21.35	19.12	3.36	
HN (5^2)	s	0.95	0.49	1.67	

To evaluate the credible interval of fitted lines, the posterior predictive distribution is used. Posterior predictive values for $logN$ are sampled from a normal distribution with mean from Equation (4) with the best fit values for A and k, and variance equal to the best fit value s^2 (6). After generating 10,000 samples, the 95%HDI can be constructed.

$$logN \sim N\left(\mathrm{A} - k.log\sigma_a \ ; \ s^2\right) \tag{6}$$

The results for 95%HDI, generated from the posterior, are shown in Figure 7. The reference two-slope curve to 10^8 cycles, from FKM guidelines, based on the fraction of tensile strength, is also added for comparison. It is clear that the intervals are broader, but they are over the reverence line, which is supposed to be conservative. Slope k = 21.4 produces a slightly narrower credible interval. Randomly drawn batches generated from the posterior samples (three samples for each stress level) are also included. The fatigue limit with 2.5% probability of failure at 10^9 cycles is estimated as σ_1 = 79.0 MPa for data with slope k = 21.4 and σ_1 = 66.5 MPa for the other slope k = 15.0.

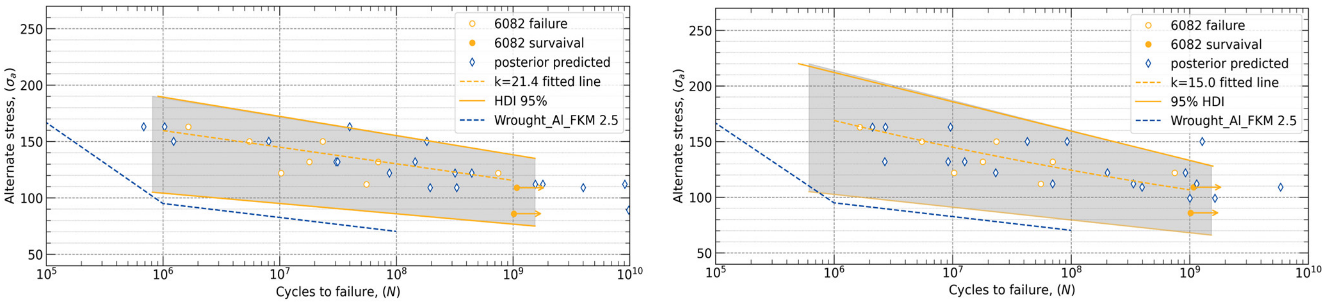

(**a**) (**b**)

Figure 7. High-density interval 95% when fitted with both slopes' experimental data. The reference two-slope curve for wrought Al alloys and random batch of generated posterior samples are included: (**a**) data fitted with slope parameter k = 21.4; (**b**) data fitted with slope parameter k = 15.0.

Better estimation of data with a relatively small sample size can be achieved using the Weibull distribution [29], for example, replacing the Normal distribution with the two-parameter Weibull in the likelihood function (4) as in [26], or using the Castillo–Canteli model with the three-parameter Weibull distribution [30]. This model maintains compatibility between the cumulative distribution functions (CFD) for fatigue lifetime at a given stress range and stress range at a given lifetime. It includes N_0 and $\Delta\sigma_0$ parameters, which give the horizontal and vertical asymptotes, where the horizontal one can be interpreted as fatigue endurance strength. In [31,32], it is shown that this model can be used for describing two-slope data from HCF and VHCF, marked as external and internal crack, combining two Weibull distributions.

With the Castillo–Canteli model, given with Equation (6), the curved lines with equal probability of failure P_f can be plotted.

$$F(N, \Delta\sigma) = 1 - \exp\left[-\left(\frac{\log \frac{N}{N_0} log \frac{\Delta\sigma}{\Delta\sigma_0} - \lambda}{\delta} \right)^{\beta} \right], \quad (7)$$

where $F(N, \Delta\sigma)$—CFD of Weibull distribution; $N_0, \Delta\sigma_0$-threshold values $\Delta\sigma_0$—indicator for the endurance limit at $N \to \infty$; λ, δ, β—location, scale and shape parameters of Weibull distribution.

Curves with probability of failure P_f = *2.5%*, *50%*, *97.5%* are shown in Figure 8. They fit the experimental data well.

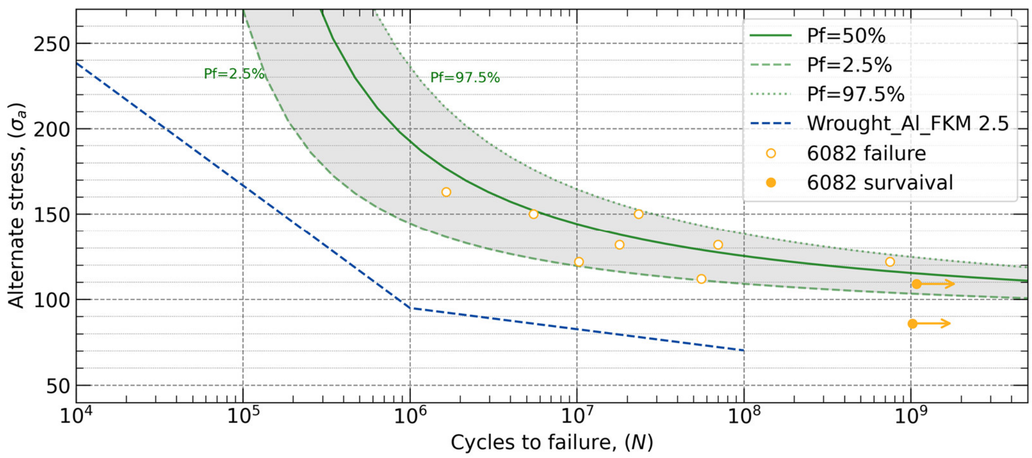

Figure 8. P-S-N fatigue curves with Pf = 2.5, 50, 97.5%, calculated with Castillo–Canteli model.

The best fit parameters inferred with the ProFatigue software [33] are given in Table 5. From the P_f = 2.5% curve, the fatigue limit at 10^9 cycles is calculated to be σ_1 = 103 MPa and the horizontal asymptote is at 84.3 MPa, which can be used as an endurance limit. As expected, this model gives the best fit of all models supposed.

Table 5. Best fit parameter of Castillo–Canteli model for AW 6082-T6.

Tested Material	N_0	$\Delta\sigma_0$, MPa	λ	δ	β
6082-T6	13,666	84.3	0.22	3.52	7.18

3.3. Fracture Morphology

The fatigue test is stopped when the resonant frequency drops by about 200–400 Hz and the required strain amplitudes cannot be reached. Currently, a fatigue crack is developed, but the specimen is not completely broken. To investigate the fracture, surface specimens were post-broken on a universal tensile testing machine.

The fractured surfaces of some specimens are studied by SEM. The overall view and selected details from the surface of a specimen, which fatigued at σ_a = 122 MPa and failed at $N = 1.03 \times 10^7$ cycles, are shown in Figure 9. The fatigue and the fast fracture zones are clearly visible, as shown in Figure 9c. The initiation of the fatigue crack is in a place with a local property fluctuation in the presence of surface defects or inclusions. Figure 9e,f show surface details in the zone of the crack initiation, where the subsurface inclusions are visible. Another site of a small crack initiation, presented in Figure 9a, shows deformation slip lines, which cannot bypass the "wall" of precipitates, and the crack growth is arrested. The direction of the main crack growth is 45° to the applied force, as shown in Figure 9c. The surface details with higher magnification show that in the crack growth zone, cleavage transgranular fracture is dominant, as shown in Figure 9d. Lines of plastic deformation, mainly by twining, which is a typical deformation mechanism in this type of material, are registered. Microvoids on a substructure grain, formed by coalescence of defects around the very fine dispersoids, are visible. Small fractions of voids and dimples, formed around the grain boundaries, due to the presence of grain boundary precipitate, can also be observed. In fast fracture zones, the fracture is predominantly intergranular. Figure 9b shows a detail, where precipitate on grain boundaries and cracking between the grains are visible. A similar fracture mode, after ultrasonic fatigue test at 20 kHz of Al-Mg-Si alloy 6061, is described in [34].

In Figure 10, another specimen is shown. Its fatigue life is $N = 5.50 \times 10^7$ cycles at higher amplitude stress. Here, in the fatigue crack propagation area, various fracture modes can be found, as shown in Figure 10a. Higher magnification detail in Figure 10b shows transition between the cleavage fatigue crack propagation area, where the fracture type is brittle trans granular, and the remaining area, with typical ductile-type fracture with dimples, is visible. In the surface detail from the crack origin, microcracks around big inclusion particles (Figure 10d) and brittle fracture with extrusions are registered (Figure 10d).

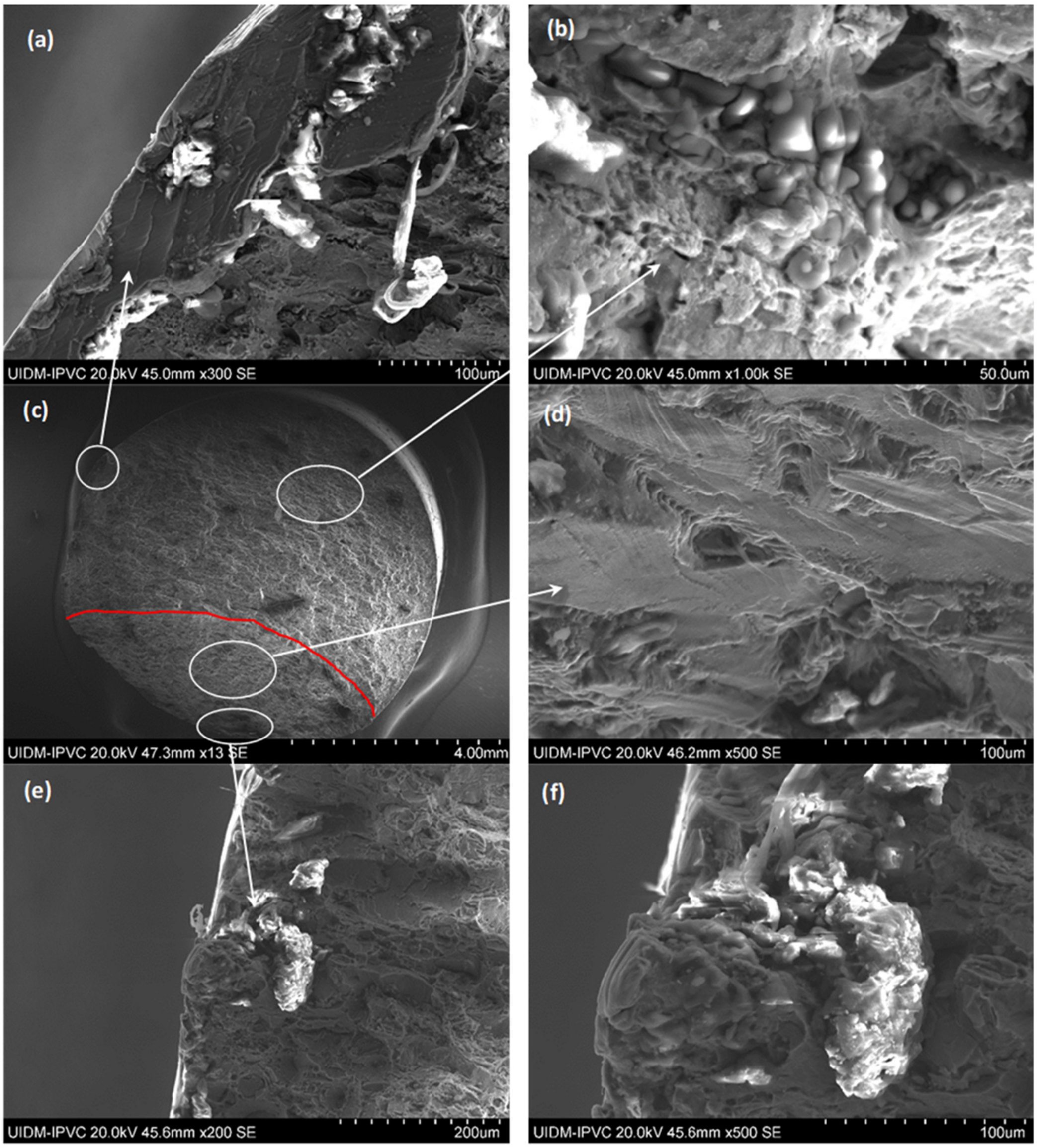

Figure 9. SEM micrographs AW 6082-T6. Fracture surface of specimen, broken at $N = 1.03 \times 10^7$ at amplitude stress σa = 122 MPa: (**a**) surface detail of small crack initiation; (**b**) detail from fast fracture zone showing intergranular fracture and precipitates around grain boundaries; (**c**) overall view of fractured surface; (**d**) detail from fatigue crack development zone shows cleavage trans crystal fracture with visible deformation slip lines; (**e**,**f**) surface details from crack origin zone.

Comparing both specimens, it is evident that the microstructure controls fatigue life. As stated in [35], the hardness of α-Al matrix is lower in peak aged condition, which activates plastic deformation by dislocation glide even at low amplitude stresses, used in VHCF testing. Fine semi-coherent dispersoids are not capable of altering the dislocation glide. This mechanism leads to localized plastic deformation, and the crack grows faster in the most favorable direction of maximal shear stress, which in pure tension–compression are planes, rotated at 45° from the axial force direction. When precipitates become larger, predominately non-coherent dislocations are more likely to bypass these particles rather than cut through them. As a result, the dislocations activate multiple slip systems, leading to a more uniform deformation at the crack tip. This results in normal-stress-controlled crack propagation [36].

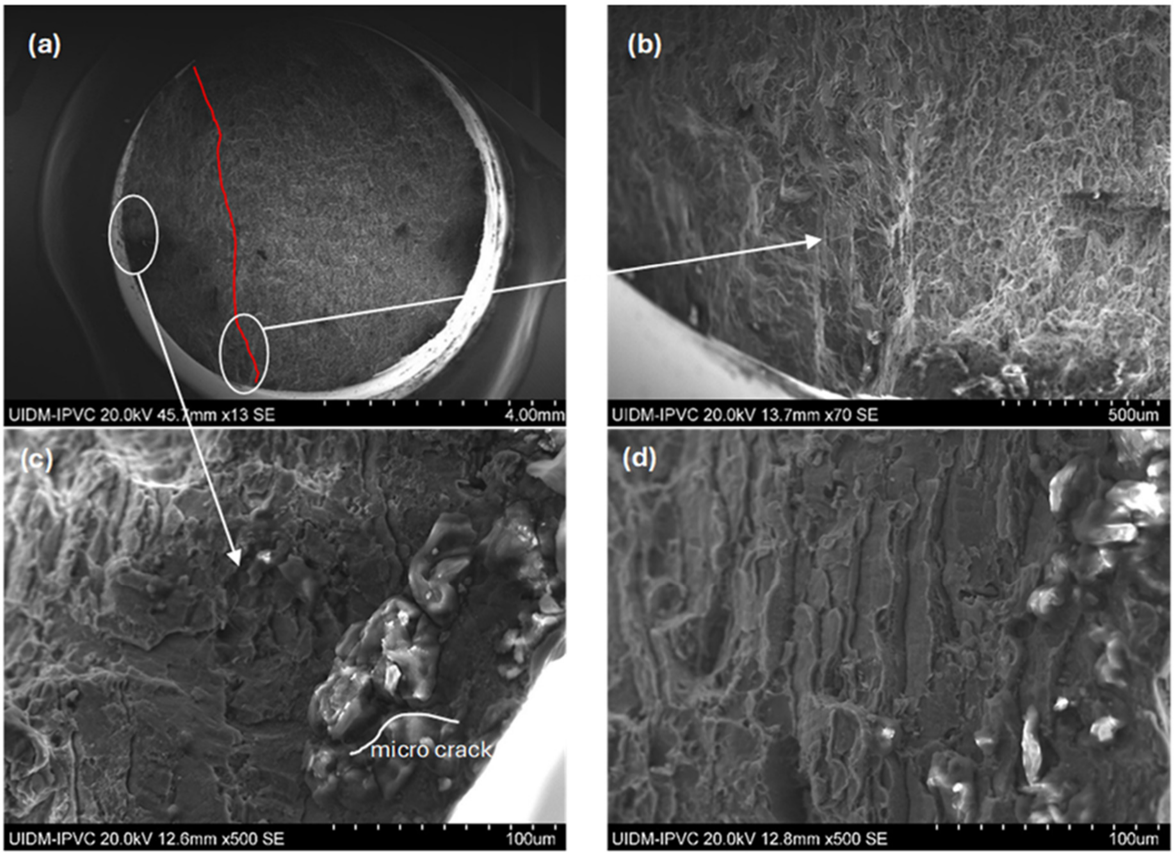

Figure 10. SEM micrographs AW 6082-T6. Fracture surface of specimen, broken at $N = 5.50 \times 10^7$ at amplitude stress σ_a = 132 MPa: (**a**) overall view of fracture surface, red line separates fatigue and fast fracture zones; (**b**) detail from transition zone, fatigue crack grows predominantly trans-crystal, but the fast fracture zone is ductile with dimples; (**c**) detail from crack initiation site; (**d**) detail from fatigue crack development zone.

4. Conclusions

The custom design of ultrasonic of ultrasonic resonance fatigue machine with working frequency 20 kHz, equipped with a custom-made Ti6Al4V Bezier sonotrode with amplification factor 1:6, capable of developing displacement amplitudes, needed for the fatigue testing of aluminum alloy 6082, is developed.

Fatigue testing in the very high fatigue cycle (VHCF) range up to 10^9 cycles of EN AW6082-T6 in tension–compression mode with symmetrical loading cycle(R = −1) is carried out. For this test specimen, a hemispherical stress concentrator is designed, based on the dynamic Young's modulus (71.3 GPa) determined by IET and the density, measured by the water displacement method 2707 kg/m^3. The specimen design is proved by FEM model.

Results from the fatigue test show that there is a decrease in the fatigue strength of about 60 MPa between 10^6 and 10^9 cycles. The S-N Wohler line, based on a Basquin equation, with slope parameter k = 21.4, fits the experimental data, but there is high scattering, resulting in broad credible intervals. The Castell–Canteli model with the three-parameter Weibull distribution is found to give better results for the relatively small sample size, such as our experimental data. By fitting this model, the fatigue limit at 10^9 cycles is estimated to σ_l = 104 MPa with probability of failure 2.5%, and the "endurance strength" at $N \to \infty$ is estimated to σ_w = 84 MPa.

The fatigue fractures are predominately initiated from the surfaces of the specimens. Cleavage morphology and trans granular crack growth path with clear slip lines in the 45° shear direction are registered on a specimen, which failed earlier than expected. The other specimen, which fatigued at slightly higher amplitude stress and reached a higher number of cycles, shows mixed morphology with trans granular and intergranular fracture modes.

Supplementary Materials: The following supporting information can be downloaded at: https://www.mdpi.com/article/10.3390/met15020127/s1, Report from ProFatigue software S1: PROJECT_ProFatigue_AW6082T6.pdf.

Author Contributions: Conceptualization, D.M.D. and S.D.S.; methodology, D.M.D., S.D.S. and A.M.S.C.; software, D.M.D., S.D.S. and A.M.S.C.; validation, D.M.D.; formal analysis, D.Y.M. and D.M.D.; investigation, D.M.D. and D.Y.M.; resources, S.D.S. and A.M.S.C.; data curation, D.Y.M.; writing—original draft preparation, D.M.D. and D.Y.M.; writing—review and editing, S.D.S. and A.M.S.C.; visualization, D.M.D., D.Y.M. and S.S; supervision, D.M.D.; project administration, D.M.D. and A.M.S.C.; funding acquisition, D.M.D. All authors have read and agreed to the published version of the manuscript.

Funding: This research was funded by Bulgarian Science Research Fund, grant number КП-06-H67/12 from 13.12.2022 entitled: Modelling of Gigacycle Fatigue Behavior of Materials.

Data Availability Statement: The original contributions presented in the study are included in the article/supplementary materials, further inquiries can be directed to the corresponding author.

Acknowledgments: The authors would like to thank João C.C. Abrantes and his scientific group from metallography laboratory of IPVC, Portugal for the support with SEM investigations.

Conflicts of Interest: The authors declare no conflicts of interest.

References

1. Bathias, C. There is no infinite fatigue life in metallic materials. *Fatigue Fract. Eng. Mater. Struct.* **1999**, *22*, 559–565. [CrossRef]
2. Höppel, H.W.; Saitova, L.R.; Grieß, H.J.; Göken, M. Surface roughening and fatigue behaviour of pure aluminum with various grain size in the VHCF regime. In Proceedings of the VHCF-4-4th International Conference on Very High Cycle Fatigue, Ann Arbor, MI, USA, 19–22 August 2007; pp. 59–66.
3. Mughrabi, H.; Allison, J.; Jones, J.W.; Ritchie, R.O.; Larsen, J.M.; Stanzl-Tschegg, S. Fatigue Damage Evolution in Ductile Single-phase Face-Centred Cubic Metals in the UHCF-Regime Fourth International Conference on Very High Cycle Fatigue Edited FATIGUE DAMAGE EVOLUTION IN DUCTILE SINGLE-PHASE FACE-CENTRED CUBIC METALS IN THE UHCF-REGIME. 2007. Available online: https://www.researchgate.net/publication/283868703 (accessed on 12 December 2024).
4. Pyttel, B.; Schwerdt, D.; Berger, C. Very high cycle fatigue—Is there a fatigue limit? *Int. J. Fatigue* **2011**, *33*, 49–58. [CrossRef]
5. Sharma, A.; Oh, M.C.; Ahn, B. Recent advances in very high cycle fatigue behavior of metals and alloys—A review. *Metals* **2020**, *10*, 1200. [CrossRef]
6. Caivano, R.; Tridello, A.; Chiandussi, G.; Qian, G.; Paolino, D.; Berto, F. Very high cycle fatigue (VHCF) response of additively manufactured materials: A review. *Fatigue Fract. Eng. Mater. Struct.* **2021**, *44*, 2919–2943. [CrossRef]
7. Schwerdt, D.; Pyttel, B.; Berger, C. Fatigue strength and failure mechanisms of wrought aluminium alloys in the VHCF-region considering material and component relevant influencing factors. *Int. J. Fatigue* **2011**, *33*, 33–41. [CrossRef]
8. Cremer, M.; Zimmermann, M.; Christ, H.-J. High-frequency cyclic testing of welded aluminium alloy joints in the region of very high cycle fatigue (VHCF). *Int. J. Fatigue* **2013**, *57*, 120–130. [CrossRef]
9. Leitgeb, A.; Gaenser, H.; Eichlseder, W. Fracture Modeling of S/N curves for flawed materials in the VHCF regime. In Proceedings of the ECF17: Multilevel Approach to Fracture of Materials, Components and Structures, Brno, Czech Republic, 2–5 September 2008; pp. 843–850.
10. Mrówka-Nowotnik, G.; Sieniawski, J.; Wierzbiñska, M. Intermetallic phase particles in 6082 aluminium alloy. *Arch. Mater. Sci. Eng.* **2007**, *28*, 69–76.
11. Mrówka-Nowotnik, G.; Sieniawski, J.; Nowotnik, A. Effect of Heat Treatment on Tensile and Fracture Toughness Properties of 6082 alloy. *J. Achiev. Mater. Manuf. Eng.* **2009**, *32*, 162–170.
12. Marioara, C.D.; Andersen, S.J.; Zandbergen, H.W.; Holmestad, R. The Influence of Alloy Composition on Precipitates of the Al-Mg-Si System. *Met. Mater. Trans. A* **2005**, *36*, 691–702. [CrossRef]
13. Hu, Z.; Zheng, J.; Pang, Q.; Sun, Q.; Zhao, N. Influence of strain rates and aging time on microstructure and hardness of integrally compressed 6082 aluminum alloy. *J. Mater. Res. Technol.* **2023**, *27*, 826–838. [CrossRef]
14. Sakai, T.; Nakagawa, A.; Oguma, N.; Nakamura, Y.; Ueno, A.; Kikuchi, S.; Sakaida, A. A review on fatigue fracture modes of structural metallic materials in very high cycle regime. *Int. J. Fatigue* **2016**, *93*, 339–351. [CrossRef]

15. Bach, J.; Höppel, H.; Prell, M.; Göken, M. Crack initiation mechanisms in AA6082 fatigued in the VHCF-regime. *Int. J. Fatigue* **2014**, *60*, 23–27. [CrossRef]
16. Montagnoli, F.; Invernizzi, S.; Carpinteri, A. VHCF ultrasonic tests on EN AW-6082 aluminum alloy samples over a wide dimensional range. *Fatigue Fract. Eng. Mater. Struct.* **2023**, *46*, 3099–3117. [CrossRef]
17. Cui, S.; Tian, F.; Ma, R.; Yu, Y.; Xu, L. Study on the Morphology, Microstructure, and Properties of 6082-T6 Aluminum Alloy Joints in MIG Welding. *Metals* **2023**, *13*, 1245. [CrossRef]
18. *ISO 6892-1:2019*; Metallic materials—Tensile testing—Part 1: Method of test at room temperature. International Organization for Standardization: Geneva, Switzerland, 2019.
19. Jacquemain, V.; Ranc, N.; Cheuleu, C.; Michel, V.; Favier, V.; Castelnau, O.; Vinci, D.; Thiaudiere, D.; Mocuta, C. Estimation of stress in specimens loaded with ultrasonic fatigue machines. *Int. J. Fatigue* **2021**, *153*, 106474. [CrossRef]
20. Biran, A. Front Matter. In *Geometry for Naval Architects*; Elsevier: Amsterdam, The Netherlands, 2019; pp. i–iii.
21. Kaldashev, T. Development of a parametric program for processing a hyperbolic surface on a lathe machine. *Environ. Technol. Resour. Proc. Int. Sci. Pract. Conf.* **2019**, *3*, 70–73. [CrossRef]
22. He, T.; Ye, X.Q.; Zhao, Y. Optimization design for ultrasonic horn with large amplitude based on genetic algorithm. *J. Vibroeng.* **2015**, *17*, 1157–1168.
23. Karolczuk, A.; Kurek, M.; Łagoda, T. Fatigue life of Aluminium alloy 6082 t6 under constant and variable amplitude bending with torsion. *J. Theor. Appl. Mech.* **2015**, *53*, 421–430. [CrossRef]
24. Bathias, C.; Paris, P.C. *Gigacycle Fatigue in MechanicalPractice*; Informa UK Limited: London, UK, 2004.
25. Zhao, Z.; Zhang, F.; Dong, C.; Yang, X.; Chen, B. Initiation and Early-Stage Growth of Internal Fatigue Cracking Under Very-High-Cycle Fatigue Regime at High Temperature. *Met. Mater. Trans. A* **2020**, *51*, 1575–1592. [CrossRef]
26. Zou, Q.; Wen, J. Bayesian model averaging for probabilistic S-N curves with probability distribution model form uncertainty. *Int. J. Fatigue* **2023**, *177*, 107955. [CrossRef]
27. Abril-Pla, O.; Andreani, V.; Carroll, C.; Dong, L.; Fonnesbeck, C.J.; Kochurov, M.; Kumar, R.; Lao, J.; Luhmann, C.C.; Martin, O.A.; et al. PyMC: A modern, and comprehensive probabilistic programming framework in Python. *PeerJ Comput. Sci.* **2023**, *9*, e1516. [CrossRef] [PubMed]
28. Rennert, R.; Vormwald, M.; Esderts, A. FKM-Guideline "analytical strength assessment"—Background and current developments. *Int. J. Fatigue* **2023**, *182*, 108165. [CrossRef]
29. Barbosa, J.F.; Júnior, R.C.S.F.; Correia, J.A.; De Jesus, A.M.; Calçada, R. Analysis of the fatigue life estimators of the materials using small samples. *J. Strain Anal. Eng. Des.* **2018**, *53*, 699–710. [CrossRef]
30. Castillo, E.; Canteli, A.C.F. *A Unified Statistical Methodology for Modeling Fatigue Damage*; Springer Nature: Dordrecht, The Netherlands, 2009.
31. Muniz-Calvente, M.; Fernández-Canteli, A.; Pyttel, B.; Castillo, E. Probabilistic assessment of VHCF data as pertaining to concurrent populations using a Weibull regression model. *Fatigue Fract. Eng. Mater. Struct.* **2017**, *40*, 1772–1782. [CrossRef]
32. Pyttel, B.; Canteli, A.F.; Ripoll, A.A. Comparison of different statistical models for description of fatigue including very high cycle fatigue. *Int. J. Fatigue* **2016**, *93*, 435–442. [CrossRef]
33. Fernández-Canteli, A.; Przybilla, C.; Nogal, M.; Aenlle, M.L.; Castillo, E. ProFatigue: A software program for probabilistic assessment of experimental fatigue data sets. *Procedia Eng.* **2014**, *74*, 236–241. [CrossRef]
34. Wang, Q.; Lib, T.; Zenga, X. Gigacycle fatigue behavior of high strength aluminum alloys. *Procedia Eng.* **2010**, *2*, 65–70. [CrossRef]
35. Höppel, H.W.; Prell, M.; May, L.; Göken, M. Influence of grain size and precipitates on the fatigue lives and deformation mechanisms in the VHCF-regime. *Procedia Eng.* **2010**, *2*, 1025–1034. [CrossRef]
36. Bülbül, F.; Kirsten, T.; Wicke, M.; Zimmermann, M.; Brückner-Foit, A.; Christ, H.-J. Crack growth behaviour of aluminium wrought alloys in the Very High Cycle Fatigue regime. *MATEC Web Conf.* **2018**, *165*, 20007. [CrossRef]